THE JOURNAL OF PHYSICAL CHEMISTRY Letters

pubs.acs.org/JPCL Letter

Photoexcitation Induced Ultrafast Nonthermal Amorphization in Sb_2Te_3

Subodh C. Tiwari, Rajiv K. Kalia, Aiichiro Nakano, Fuyuki Shimojo, Priya Vashishta, and Paulo S. Branicio*

Cite This: J. Phys. Chem. Lett. 2020, 11, 10242−10249 Read Online

ACCESS | Metrics & More | Article Recommendations | Supporting Information

ABSTRACT: Phase-change materials are of great interest for low-power high-throughput storage devices in next-generation neuromorphic computing technologies. Their operation is based on the contrasting properties of their amorphous and crystalline phases, which can be switched on the nanosecond time scale. Among the archetypal phase change materials based on Ge−Sb−Te alloys, Sb_2Te_3 displays a fast and energy-efficient crystallization−amorphization cycle due to its growth-dominated crystallization and low melting point. This growth-dominated crystallization contrasts with the nucleation-dominated crystallization of $Ge_2Sb_2Te_5$. Here, we show that the energy required for and the time associated with the amorphization process can be further reduced by using a photoexcitation-based nonthermal path. We employ nonadiabatic quantum molecular dynamics simulations to investigate the time evolution of Sb_2Te_3 with 2.6, 5.2, 7.5, 10.3, and 12.5% photoexcited valence electron−hole carriers. Results reveal that the degree of amorphization increases with excitation, saturating at 10.3% excitation. The rapid amorphization originates from an instantaneous charge transfer from Te-*p* orbitals to Sb-*p* orbitals upon photoexcitation. Subsequent evolution of the excited state, within the picosecond time scale, indicates an Sb−Te bonding to antibonding transition. Concurrently, Sb−Sb and Te−Te antibonding decreases, leading to formation of wrong bonds. For photoexcitation of 7.5% valence electrons or larger, the electronic changes destabilize the crystal structure, leading to large atomic diffusion and irreversible loss of long-range order. These results highlight an ultrafast energy-efficient amorphization pathway that could be used to enhance the performance of phase change material-based optoelectronic devices.

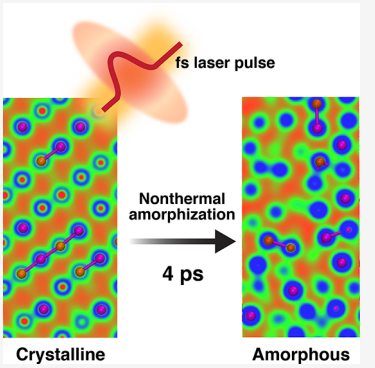

With ever-increasing demand for faster electronics and physical and manufacturing constraints of current technologies, there is a growing interest in new materials that enable hardware acceleration and are suitable for new computing paradigms.[1−5] Phase change materials (PCMs) are one of the most promising materials to fulfill the role of both high throughput nonvolatile memory devices[6−9] and brain inspired neuromorphic computing.[10−12] Devices based on PCMs leverage the contrasting optoelectronic properties between their amorphous and crystalline phases.[13,14]

Ge−Sb−Te alloys, an archetypical phase change material family, have been widely investigated both experimentally and theoretically due to their rapid crystalline−amorphous transition.[8] Specifically, $Ge_2Sb_2Te_5$ can be switched from crystalline to amorphous in a short time span of 10 ns by applying short laser or electric pulses. On the other hand, the $Ge_2Sb_2Te_5$ crystallization process requires an order of magnitude longer time. Sb_2Te_3, another chalcogenide PCM, has shown a faster phase change cycle and lower power consumption compared to $Ge_2Sb_2Te_5$ due to its growth-dominated crystallization and lower melting point.[15,16] In contrast with Sb_2Te_3 growth-dominated crystallization, the crystallization kinetics of $Ge_2Sb_2Te_5$ is nucleation-dominated.[17−19] Despite the outstanding performance of Sb_2Te_3, its low electrical resistivity and thermal stability hinders its use in practical applications. Improvements in thermal stability and enhancement of the crystallization speed were reported with the use of doping.[19] In particular, amorphization in Sb_2Te_3 is hindered by its low electric resistivity. The transition time from crystalline to amorphous states could be reduced by employing photoexcitation by stronger and short laser pulses, i.e. femtosecond lasers, because such processes are unaffected by the low electric resistivity of the material.

Photoexcitation amorphization is a common phenomenon where materials undergo amorphization as a result of electronic excitation followed by electron−phonon coupling, gradual heat up of the lattice and melting, followed by quenching.[8,20] This method is employed in rewritable CD, DVD, and Blu-ray technologies. By employing strong femtosecond laser pulses, high electronic excitations can be achieved, leading to the

Received: August 18, 2020
Accepted: November 12, 2020

https://dx.doi.org/10.1021/acs.jpclett.0c02521
J. Phys. Chem. Lett. 2020, 11, 10242−10249

instability of materials' crystalline structure.[21] This opens a path for direct nonthermal amorphization, i.e. loss of long-range order without involving a melt-quench process.[22−24] Time-resolved optical measurements and theoretical studies reported ultrafast subpicosecond amorphization induced by femtosecond lasers in different materials.[23−27] The ultrafast time-scale and low energy involved in the nonthermal amorphization process are highly sought after for energy efficient and high transfer rate devices.[28] Previous theoretical studies estimate that about 11% valence electron excitation is required to induce lattice instability in covalently bonded silicon and gallium arsenide.[21,29,30] The crystalline structure of Sb_2Te_3, as well as other Ge−Sb−Te alloys, is stabilized by a network of resonant bonds. It is still to be determined, the exact electronic and ionic processes leading to the destabilization of Sb_2Te_3 crystalline structure and resulting nonthermal amorphization by femtosecond laser photoexcitation.

Photoexcitation induced nonthermal amorphization of phase-change materials has been considered in experimental and theoretical investigations.[31] However, a description of the atomic and electronic mechanisms leading to the time dependent nonthermal amorphization processes are still to be reported. Here, we present first-principles nonadiabatic quantum molecular dynamics (NAQMD) simulations that unambiguously demonstrate nonthermal, picosecond amorphization of Sb_2Te_3 induced by photoexcitation. Furthermore, detailed analysis elucidates the electronic and lattice-dynamic mechanisms underlying the rapid amorphization process. These novel physical insights involve an instantaneous electronic excitation process, evolution of electronic-state characters, their effect on the Sb_2Te_3 bonding, electron−phonon coupling, and diffusion processes resulting in loss of long-range order. This manuscript also highlights the real-time charge dynamics and its effect on bond-overlap population of Sb_2Te_3 during the amorphization process.

To systematically study the effects of photoexcitation in Sb_2Te_3 and the possibility of nonthermal amorphization, we perform NAQMD simulations on a supercell consisting of 180 atoms with n = 2.6, 5.2, 7.5, 10.3, and 12.5% valence electrons in excited states, corresponding to a carrier density of 0.45, 0.91, 1.33, 1.82, and 2.21 ($\times 10^{22}$ cm^{-3}), respectively. Fluence and total energy required for excitation for n = 7.5% is reported in Supporting Information. The crystalline structure is initially thermalized at 300 K by using a Nose-Hoover thermostat for 2.4 ps.

After initial thermalization, we excite the valence electrons and simulate the evolution of the excited states at a constant temperature of 500 K within the canonical ensemble (NVT). The rationale for this simulation setup is to highlight the effect of photoexcitation in the structural stability of Sb_2Te_3, assuming that the slow buildup of heat from local photoexcitation is readily dissipated throughout a large experimental sample. Simulation details and rationale for the choice of temperature are provided in Supporting Information. Figure 1a shows the Sb_2Te_3 crystalline supercell at 500 K temperature. Figures 1b−d show the structure of Sb_2Te_3 after photoexciting n = 5.2, 7.5, and 10.3% of the valence electrons and performing dynamics for 4.2 ps, respectively. Additional figures highlighting the Sb_2Te_3 structures for photoexcitation with n = 2.6 and 12.5% are shown in Supporting Information Figure S1. As one can observe, excitation of n = 2.6% (Figure 1b) does not affect the crystalline order of the structure within the time evolution considered. In contrast, for n = 10.3% excitation,

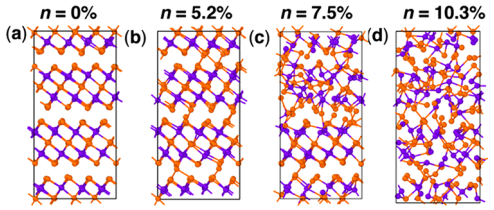

Figure 1. Sb_2Te_3 simulation supercell structures: (a) structure of Sb_2Te_3 at 500 K with no excitation and (b−d) structure of Sb_2Te_3 after 4.2 ps excited state dynamics with 5.2, 7.5, and 10.3% excited valence electrons, respectively. Purple and orange spheres correspond to Sb and Te atoms, respectively.

Figure 1d indicates loss of long-range order, which also applies for n = 12.5%, as shown in Supporting Information Figure S1b. Considering that the melting temperature of Sb_2Te_3 is 890 K,[32] the result suggests an amorphization of the structure via a path not involving the usual melting-quenching, i.e. a nonthermal amorphization. For n = 7.5%, Figure 1c indicates a local rearrangement of the structure, i.e. formation of several Sb−Sb and Te−Te wrong bonds and partial amorphization of system. For n = 5.2%, one can note the formation of few wrong bonds, while most of the structure remains crystalline.

To obtain further insights into the excited dynamics leading to the contrasting results illustrated in Figures 1b−d, we calculate the atomic mean square displacement (MSD) for all aforementioned cases. The MSD results for Sb atoms are shown in Figure 2. As a reference point, we performed a

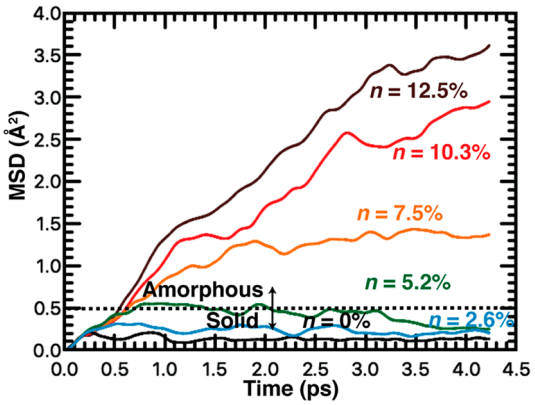

Figure 2. Mean square displacement of Sb as a function of time during simulations at T = 500 K. Cyan, green, orange, red, and brown curves correspond to excitation of n = 2.6, 5.2, 7.5, 10.3, and 12.5%, respectively. The black curve corresponds to the adiabatic MD simulation. n indicates the percentage of excited electrons out of the total valence electrons. The black dashed line shows the highest mean square displacement at 800 K.

simulation with n = 0%, as shown by the black line in Figure 2, which indicates no atomic diffusion. Results for n = 2.6%, shown by the cyan line in Figure 2, closely follows the reference curve for n = 0%, indicating no diffusion and implying no change in structure. In contrast, the green curve in Figure 2, corresponding to the simulation with n = 5.2% excitation, shows a residual MSD of 0.6 Å^2, which is small yet clearly higher than that of n = 0% and n = 2.6%. Corresponding Figure 1b for n = 5.2% suggests the higher residual MSD is a result of picosecond induced localized disorder in the structure. To be noted, after 3.0 ps, the MSD curve displays a notable decrease, indicating the restoration of crystalline

https://dx.doi.org/10.1021/acs.jpclett.0c02521
J. Phys. Chem. Lett. 2020, 11, 10242−10249

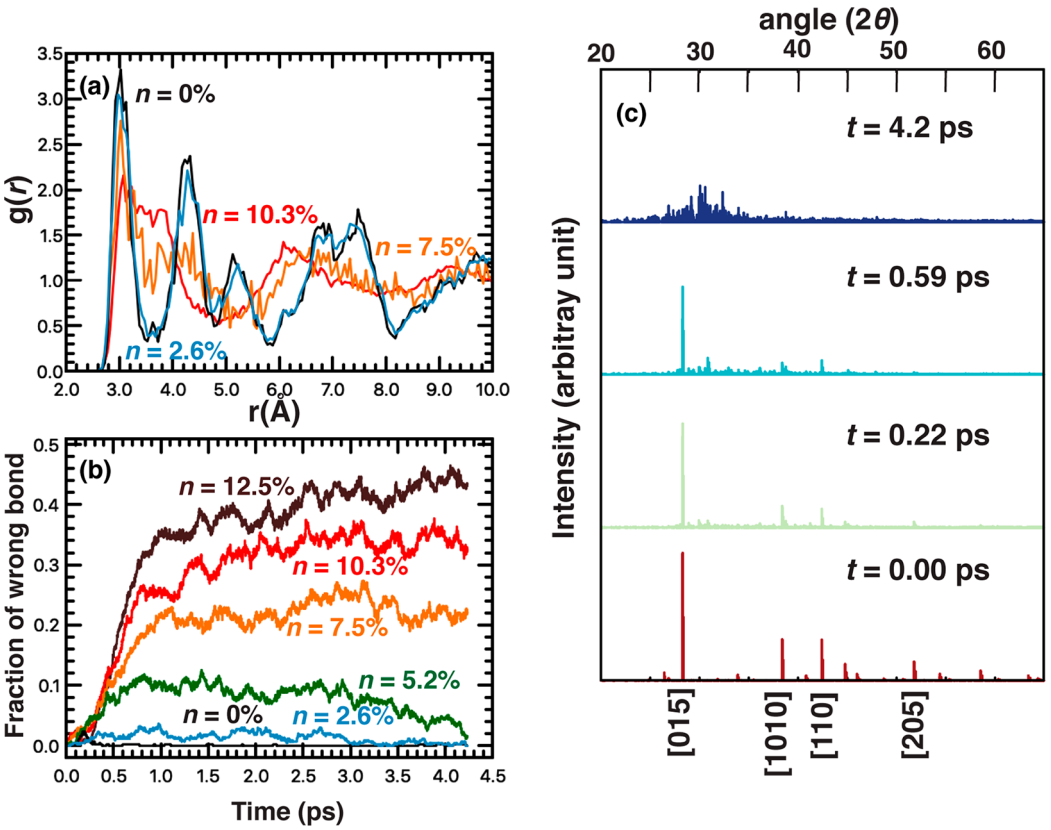

Figure 3. Analysis of the structural evolution. (a) Total radial distribution function as a function of excitation level. (b) Evolution of the fraction of wrong bonds for different excitation levels. (c) Evolution of simulated diffraction pattern for n = 10.3% excitation.

arrangement. Results from simulations with higher excitation levels, n = 10.3 and 12.5%, shown by the red and brown curves, respectively, indicate a distinct behavior characterized by a sharp increase in the MSD within 3 ps time scale. That is followed by steady increase of the MSD to 3 Å^2 within 4 ps for n = 10.3% and to 3.5 Å^2 for n = 12.5%. Even though we observe large atomic displacements in the system, the lattice temperature remains below the melting point. Furthermore, local temperature calculations indicate the absence of local thermal melting, see Figure S2. For n = 7.5%, the MSD increases sharply to ∼1.3 Å^2 within 2 ps and then remains constant. That indicates that electronic excitation at n = 7.5% or higher induces large atomic diffusion. Figure 1d, for n = 10.3% excitation, shows that the induced atomic diffusion leads to widespread bond breaking and loss of the crystalline arrangement and long-range order. MSD results for Te are provided in Supporting Information Figure S3. Quantitatively, MSD for Te atoms is lower than that for Sb atoms due to heavier mass of the Te atom. However, the diffusion trends at different excitation fractions are identical to those of Sb atoms.

To further identify the change in the structure after excited state dynamics, we perform radial distribution function (g(r)) analysis. Figure 3a shows the radial distribution function for the systems after 4.2 ps of time evolution for n = 0, 2.6, 7.5, and 10.3%. Curves for n = 5.2 and 12.5% are not shown in Figure 3a for clarity. Total and partial radial distribution functions for all excitation levels are shown in Figure S4. The first peaks of the radial distribution function are located at 3.02 and 4.32 Å, as shown in Figure 3. The first peak indicates the Sb−Te bonds, as shown in Figure S4. The latter indicates the Sb−Sb and Te−Te nearest distance. The observed strong correlation of the curves for n = 0 and 2.6% at all distances suggests the preservation of both short and long-range order. The results for n = 7.5%, shown by the orange curve in Figure 3a, indicate a well-defined first peak, suggesting the preservation of short-range order. However, the lower intensity of the first peak and the partial overlap with the second, adding a shoulder to the first peak, indicate that some loss of short and medium range order has occurred. For the n = 10.3 and 12.5% cases, a merged broad single peak appears in the g(r), suggesting a strong change in the short-range order. To further understand this short-range order change, we evaluate the fraction of wrong bonds formed during the evolution of the excited state, as shown in Figure 3b. Total wrong bonds are defined as all homoatomic bonds (Sb−Sb and Te−Te bonds). For n = 0%, we can observe that the fraction of wrong bonds remains at 0%. Beside small fluctuations the same applies to n = 2.6%. As we increase the excitation, the number of wrong bonds formed increases. For n = 5.2%, the fraction of wrong bonds remains below 10%, decreasing further below 2%, suggesting a transient change in short-range order. For higher excitation (n = 7.5, 10.3, and 12.5%), the number of wrong bonds increases dramatically to over 20%, suggesting loss of short-range order. This observation is directly correlated with the partial overlap, for n = 7.5%, and merging of the g(r) first and second peaks, for n = 10.3 and 12.5%.

A loss of long-range order is also suggested in Figure 3a. The absence of distinct third, fourth, and fifth peaks of the crystalline structure shown by the g(r) curves for n = 7.5 and 10.3% is an indication of loss of long-range order. Calculated electron diffraction pattern, Figure 3c, for the system as a function of time further supports the loss of long-range order

https://dx.doi.org/10.1021/acs.jpclett.0c02521
J. Phys. Chem. Lett. 2020, 11, 10242−10249

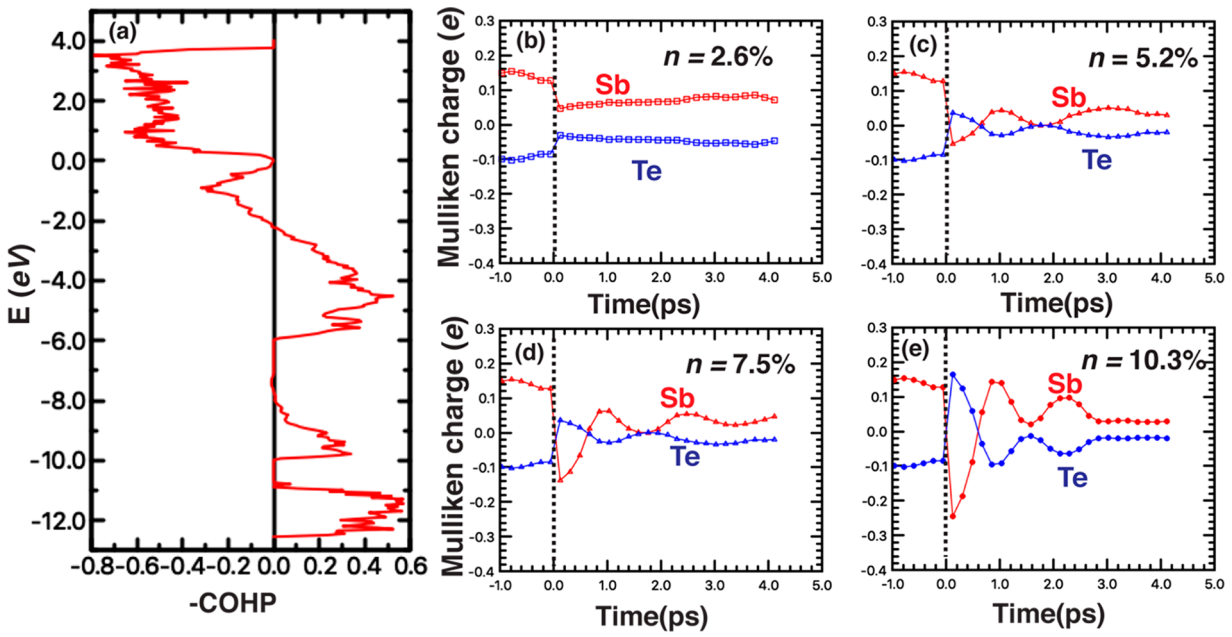

Figure 4. Effect of excitation on the Sb_2Te_3 crystal. (a) Crystal Orbital Hamiltonean Population (COHP) analysis. (b–e) Average Mulliken charge per component as a function of time. n = 2.6, 5.2, 7.5, and 10.3% excitation.

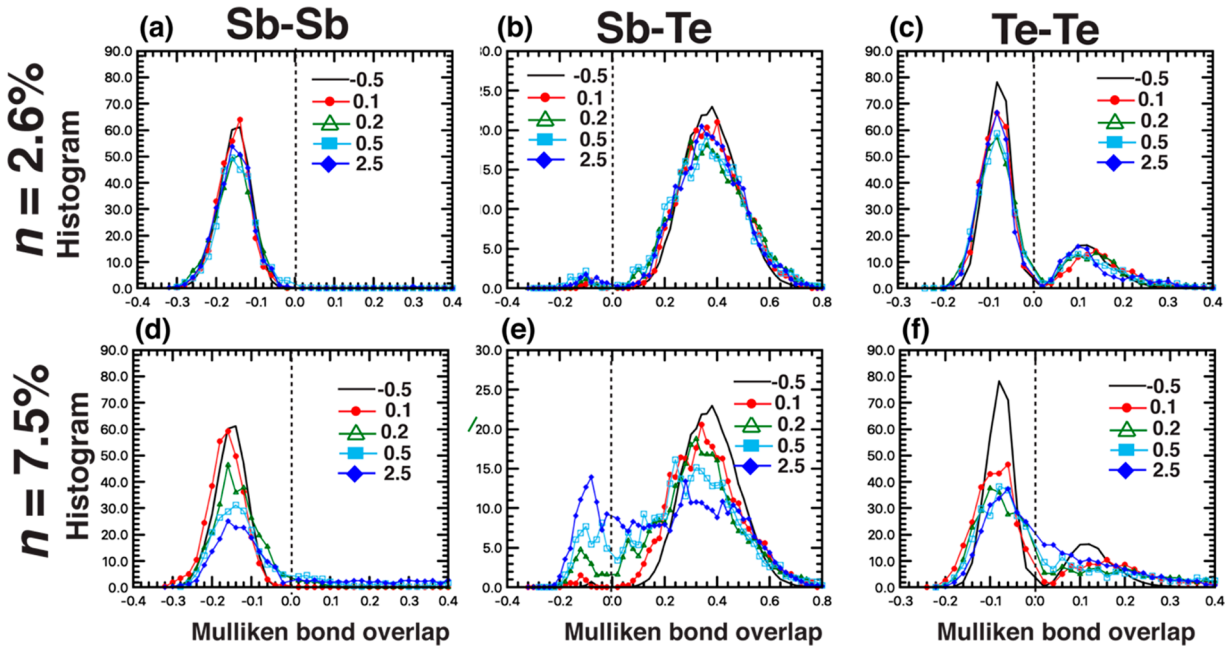

Figure 5. Evolution of Mulliken bond overlap analysis as a function of time for (a) Sb–Sb, (b) Sb–Te, and (c) Te–Te bond pairs for n = 2.6%. Similarly, panels d–f correspond to Sb–Sb, Sb–Te, and Te–Te bond pairs for n = 7.5%, respectively. The black curve corresponds to the t = −0.5 ps (before excitation). Red, green, cyan, and blue colors correspond to times t = 0.1, 0.2, 0.5, and 2.5 ps after excitation.

and formation of an amorphous system. Figure 3c shows the calculated electron diffraction pattern as a function of time for n = 10.3%. We can observe a strong peak for the [015] plane at 28.3° angle as well as lower intensity peaks for [10$\underline{1}$0], [110], and [205] planes for the initial crystalline system (at time t = 0 ps). At t = 0.59 ps after photoexcitation, the [015] peak is still well-defined, while the peak intensity for the remaining peaks of the crystalline structure declined significantly. Finally, at t = 4.2 ps, we observe the complete disappearance of the [015] peak, suggesting a complete loss of long-range order and consequent formation of an amorphous state.

To understand the effect of excitation on chemical bonding, we performed Crystal Orbital Hamiltonian Population (COHP) analysis for the Sb_2Te_3 crystal.[33] The calculated COHP curve is shown in Figure 4a. Details on the COHP analysis are provided in the Supporting Information. COHP analysis shows that bands near valence band maximum (VBM) are antibonding. Thus, excitation of electrons from the valence band maximum does not destabilize the crystal. However, strong excitation leads to removal of electrons from Sb–Te bonding orbitals, leading to destabilization of the crystalline order. To understand the evolution of electronic states induced

https://dx.doi.org/10.1021/acs.jpclett.0c02521
J. Phys. Chem. Lett. 2020, 11, 10242–10249

by the photoexcitation process, we evaluate the charge transfer between atomic species by calculating the average Mulliken charge per atomic species during the excited state dynamics. The results for n = 2.6, 5.2, 7.5, and 10.3% are shown in Figures 4b−e. In all cases, the plots show a sharp charge transfer from Te to Sb at time t = 0 ps, the instantaneous photoexcitation time. Negative/positive times in the plots indicate dynamics prior/post photoexcitation. At n = 2.6% excitation, the results in Figure 4a show a nearly identical Mulliken charge for both species after excitation. The evolution of the excited states indicate that the ground state is mostly recovered in a short period of 4 ps. Given that the structural result from Figures 2 and 3 suggest a crystalline state, we expect a full recovery of the ground state for both Sb and Te species in sufficiently longer relaxation. The results for n = 5.2% excitation, shown in Figure 4b, indicates an almost reversed average charge after photoexcitation compared to their ground state. Similar to the n = 2.6% case, we observe a swift partial recovery of the Sb and Te ground state charge within 4 ps of evolution. In contrast, Figure 4c shows a different behavior for n = 7.5%. At such high excitation level, the average charge reverse sign and increase in magnitude indicate a strong charge transfer from Te to Sb. In a short time span of 4 ps, a strong reversal in charge transfer occurs, even though it indicates the final steady state is distinct from the ground state. Results for n = 10.3 and 12.5% follow the same trend as n = 7.5%, as shown in Figures 4d, e and Figure S4. Bader charge analysis, shown in Figure S6, displays qualitatively the same results of charge transfer from Sb to Te atoms, as shown by the Mulliken charge analysis. However, the average charge value per atom type differs, as expected.[34]

To understand the effect of charge transfer from Te to Sb on the crystalline order, we performed Mulliken bond overlap analysis as a function of time, as shown in Figure 5. Figures 5a−c show the histogram of Mulliken bond overlap for n = 2.6% photoexcitation for Sb−Sb, Sb−Te, and Te−Te bond pairs, respectively. Before photoexcitation, at t = −0.5 ps, the reference bond overlap histograms are very well-defined, corresponding to the different bonds present in the Sb_2Te_3 crystal structure. These are represented by the black curves in Figures 5a−c. Figure 5a indicates a peak at −0.15 for the Sb−Sb bond pair, corresponding to antibonding interaction between Sb−Sb atom types. For the Sb−Te bond type (Figure 5b), we observe a peak at 0.4, corresponding to a large Sb−Te bonding interaction. For the Te−Te bond type, we observe a large peak at −0.07 and a small peak at 0.12. The antibonding peaks at −0.07 correspond to the intralayer repulsion between Te atoms, while the bonding peak at 0.12 corresponds to the interlayer interaction between Te atoms. Such interlayer bonding interaction between Te atoms is associated with the layered structure of Sb_2Te_3. The same black reference curves are shown in Figure 5d−f for n = 7.5%.

At time t = 0.1 ps after excitation, Sb−Sb histogram peaks for n = 2.6% and n = 7.5% show increased antibonding interaction, i.e., increase in peak width or height in the negative region. The negative shift of the peak location for the Sb−Sb bond type increases with excitation level (see Figure S7 for n = 5.2, 10.3, and 12.5%). The Sb−Te bond type shows a decrease in peak intensity in the bonding region, while a new peak appears in the antibonding region at −0.12, as shown in Figure 5b and 5e. In contrast with changes in Sb−Sb and Sb−Te bond types, the data shown in Figures 5c and f indicate that the Te−Te peak intensities in the negative and positive regions decrease, implying a decreased bonding interaction between Te atoms. For n = 2.6%, as the system evolves, we observe that all the aforementioned changes in excited states increasingly shift toward the ground state, as shown by the green, cyan, and blue curves in Figures 5a−c. That is consistent with the preservation of the Sb_2Te_3 crystalline structure. However, for n = 7.5%, as the system evolves, the Sb−Te bond overlap curve becomes broad and expands into the antibonding region shown by the green, cyan, and blue curves in Figure 5e. That is consistent with the scission of Sb−Te bonds. Concurrently, the two peaks displayed by Te−Te at time t = 0.1 ps merged into a broad distribution, indicating no prominent bonding or antibonding interaction (Figure 5f). The results for Sb−Sb, displayed in Figure 5d, indicate that the antibonding interaction is still prevalent, although residual bonding interaction is present. Similar changes in bond overlap for different bond types are observed for n = 5.2 and 10.3 and 12.5% (Figure S7). The combination of Sb−Te bond scission and Sb−Sb/Te−Te bond formation is consistent with the amorphization of the structure, as illustrated in Figures 1c and d.

The results presented demonstrate photoexcitation driven nonthermal amorphization in Sb_2Te_3. It is instructive to consider the electronic origin of the nonthermal amorphization path. In the Sb_2Te_3 crystalline phase, valence band maxima (VBM) are composed of a linear combination of Te p orbitals, whereas conduction band minima (CBM) are composed of a linear combination of mostly Sb p orbitals.[35] Accordingly, electronic excitation is accompanied by charge transfer from Te to Sb atoms, leading to a Sb−Te bonding to antibonding transition. This in turn drives displacement of atoms, which are directly related to the excitation magnitude. The electronic origin of such displacement has been studied both theoretically and experimentally.[36,37] Atomic displacement was linked to wave function phase flipping, where bonding orbitals become antibonding, thereby leading to Sb−Te bond scission and Te−Te bond formation. Phase flipping was hypothesized as the cause of amorphization of different resonant-bonding materials such as GeTe.[38] For low electronic excitation, phase flipping occurs randomly in the material and leads to small localized distortions in the system. In contrast, for larger excitation, e.g. n = 7.5%, a coherent phase flipping leads to rupture of Sb−Te and generation of Sb−Sb and Te−Te bonds, which only requires small thermal vibrations corresponding to temperatures below the melting point. Similar homogeneous bonding−antibonding transitions leading to nonthermal processes and lattice dynamics have also been reported to occur in $TiSe_2$.[39] The nonthermal melting of binary alloy compounds such as phase change GeTe-Sb_2Te_3 alloys is intrinsically different from that in single component covalent materials such as Ge and Si. In the latter, band-to-band transitions and electron−phonon interactions are responsible for the nonthermal amorphization processes.[40,41] It is important to note that the amorphization of the system for n = 7.5% is partial, leaving the system with regions in the crystalline state, as shown in Figure 1c. The presence of crystalline seeds in the amorphous structure are essential to enhance the crystallization process as they shorten the time associated with the crystal nucleation. Crystal precursor has shown to improve the performance of $Sc_{0.2}Sb_2Te_3$,[42] as has the priming of the amorphous structure in $Ge_2Sb_2Te_5$.[43] One may note that we chose NAQMD simulation at higher temperature to account for the interplay between thermal energy dissipation

https://dx.doi.org/10.1021/acs.jpclett.0c02521
J. Phys. Chem. Lett. 2020, 11, 10242−10249

and lattice heat-up from electron−phonon coupling. Simulation performed at higher/lower temperature than the one used (500 K) will require different carrier density. A linear relationship between amorphization and initial temperature has been proposed for tellurium.[44] However, the electronic and atomic process leading to amorphization will not be affected.

To highlight the uniqueness of the nonthermal path between the crystalline and amorphous structures of Sb_2Te_3, it is worth discussing the bonding in the amorphous structure and how it contrasts with that in the crystalline phase. The crystalline structure of Sb_2Te_3 and other phase change materials and alloys is intrinsically fragile. The primary bonding in the crystalline phase has been described as resonant.[13] However, in the amorphous phase, the primary bond is covalent. As discussed by Kolobov et al.,[25] stability of the crystalline resonant bonding demands the existence of long-range order. In addition, the resonant bonding is formed by the same *p*-orbitals that constitute the covalent structure in the amorphous phase. Small atomic displacements, such as those induced by the light excitation, may induce enough misalignment of the bonds that trigger the collapse of the crystalline order and amorphization. Interestingly, Waldecker et al. demonstrated that femtosecond laser excitation is capable of changing the optical properties of $Ge_2Sb_2Te_5$ drastically as well as noticeable changes to the crystal structure.[45] This implies that a rapid depletion of resonant bonding was directly induced by laser excitation.

Recently, the bonding in GeTe-Sb_2Te_3 alloys and other phase change materials in the crystalline phase have been described as *p*-bonded metavalent in contrast to the *p*-bonded covalent bonding of their amorphous phase.[46,47] The metavalent concept builds on the concept of hypervalent bonding in materials.[48,49] The concept of a metavalent material explains the bonding in crystals that could not otherwise be explained in terms of common bonding mechanisms such as metallic, ionic, and covalent. Electrons in metavalent bonding would not be fully localized as in covalent bonding nor fully delocalized as in metallic bonding.[46] In an "electrons shared vs electrons transferred" map, metavalent bonding would display about 0.5 to 1 electrons transferred and electrons shared in contrast with covalent and resonant bonding (more electrons shared), metallic bonding (no electrons transferred), and ionic bonding (more electrons transferred).[47] In perspective of the metavalent bonding, the nonthermal amorphization path presented in this work provides a new ultrafast mechanism to disturb crystalline Sb−Te metavalent bonding, thereby rapidly disrupting the long-range order of the structure.

In conclusion, we described a photoexcitation-based nonthermal path for amorphization of Sb_2Te_3 in this work. We employed nonadiabatic quantum molecular dynamics simulations to simulate the time evolution of Sb_2Te_3 at T = 500 K with 2.6, 5.2, 7.5, 10.3, and 12.5% photoexcited valence electron−hole carriers. The results reveal nonthermal amorphization in a picosecond time scale for excitation at and above 7.5%. The evolution of the excited state shows a Sb−Te bonding to antibonding transition driven by an instantaneous charge transfer from Te-*p* orbitals to Sb-*p* orbitals upon photoexcitation. Simultaneously, Sb−Sb and Te−Te antibonding interaction decreases, leading to the formation of wrong bonds and amorphization of the structure. Photoexcitation of 7.5% valence electrons or larger destabilize the crystal structure, leading to large atomic diffusion and irreversible loss of long-range order. These results underline an ultrafast energy-efficient pathway for the amorphization process that could be used to enhance the performance of optoelectronic devices based on phase change materials.

METHODS

In this work, we use the QXMD software to perform NAQMD simulations.[50] In quantum molecular dynamics, the trajectories of all atoms are integrated based on intermolecular forces calculated using the Hellmann−Feynman theorem in the density functional theory framework.[51−54] In NAQMD, excited state forces are computed based on the nonself-consistent Harris−Foulkes approach. The details on electron−phonon coupling in the NAQMD method are provided in the Supporting Information. The details of the NAQMD method were reported previously.[55] We employ the GGA approximation with dispersion forces calculated with the DFT-D method.[56,57] The projected argument wave (PAW) method is used in the calculation of the electronic states.[58] The dynamics of the excited states is modeled using the fewest-switches-surface-hopping method.[59−61]

ASSOCIATED CONTENT

Supporting Information

The Supporting Information is available free of charge at https://pubs.acs.org/doi/10.1021/acs.jpclett.0c02521.

Discussion on simulation setup mean square calculation, Mulliken charge and bond overlap analysis, and additional analysis for various carrier concentration in images S1−S7 (PDF)

AUTHOR INFORMATION

Corresponding Author

Paulo S. Branicio − *Collaboratory for Advanced Computing and Simulation, Mork Family Department of Chemical Engineering and Materials Science, University of Southern California, Los Angeles, California 90007, United States;* orcid.org/0000-0002-8676-3644; Email: branicio@usc.edu

Authors

Subodh C. Tiwari − *Collaboratory for Advanced Computing and Simulation, Mork Family Department of Chemical Engineering and Materials Science, University of Southern California, Los Angeles, California 90007, United States;* orcid.org/0000-0002-5516-6900

Rajiv K. Kalia − *Collaboratory for Advanced Computing and Simulation, Mork Family Department of Chemical Engineering and Materials Science, University of Southern California, Los Angeles, California 90007, United States*

Aiichiro Nakano − *Collaboratory for Advanced Computing and Simulation, Mork Family Department of Chemical Engineering and Materials Science, University of Southern California, Los Angeles, California 90007, United States;* orcid.org/0000-0003-3228-3896

Fuyuki Shimojo − *Department of Physics, Kumamoto University, Kumamoto 860-8555, Japan*

Priya Vashishta − *Collaboratory for Advanced Computing and Simulation, Mork Family Department of Chemical Engineering and Materials Science, University of Southern California, Los Angeles, California 90007, United States;* orcid.org/0000-0003-4683-429X

Complete contact information is available at:

https://dx.doi.org/10.1021/acs.jpclett.0c02521
J. Phys. Chem. Lett. 2020, 11, 10242−10249

https://pubs.acs.org/10.1021/acs.jpclett.0c02521

Author Contributions

P.S.B., A.N., P.V., F.S., and R.K.K. designed the research. S.T. performed the simulations. S.T. and P.S.B. performed the analysis and prepared the first manuscript draft. All participated in final manuscript preparation.

Notes

The authors declare no competing financial interest.

■ ACKNOWLEDGMENTS

This work was supported as part of the Computational Materials Sciences Program funded by the U.S. Department of Energy, Office of Science, Basic Energy Sciences, under Award DE-SC0014607. We would also like to thank the University of Southern California Center for Advanced Research Computing (USC-CARC) and the Argonne Leadership Computing Facility under the DOE INCITE and Aurora Early Science programs for provided computing resources

■ REFERENCES

(1) Zidan, M. A.; Strachan, J. P.; Lu, W. D. The Future of Electronics Based on Memristive Systems. *Nat. Electron.* **2018**, *1*, 22−29.

(2) Chen, X.; Zhou, Y.; Roy, V. A. L.; Han, S. T. Evolutionary Metal Oxide Clusters for Novel Applications: Toward High-Density Data Storage in Nonvolatile Memories. *Adv. Mater.* **2018**, *30*, 1−9.

(3) Lichtman, J. W.; Pfister, H.; Shavit, N. The Big Data Challenges of Connectomics. *Nat. Neurosci.* **2014**, *17*, 1448−1454.

(4) Kalinin, S. V.; Sumpter, B. G.; Archibald, R. K. Big-Deep-Smart Data in Imaging for Guiding Materials Design. *Nat. Mater.* **2015**, *14*, 973−980.

(5) Li, X.-B.; Chen, N.-K.; Wang, X.-P.; Sun, H.-B. Phase-Change Superlattice Materials toward Low Power Consumption and High Density Data Storage: Microscopic Picture, Working Principles, and Optimization. *Adv. Funct. Mater.* **2018**, *28*, 1−21.

(6) Ielmini, D.; Lacaita, A. L. Phase Change Materials in Non-Volatile Storage. *Mater. Today* **2011**, *14*, 600−607.

(7) Hamann, H. F.; O'Boyle, M.; Martin, Y. C.; Rooks, M.; Wickramasinghe, H. K. Ultra-High-Density Phase-Change Storage and Memory. *Nat. Mater.* **2006**, *5*, 383−387.

(8) Wuttig, M.; Yamada, N. Phase-Change Materials for Rewriteable Data Storage. *Nat. Mater.* **2007**, *6*, 824−832.

(9) Simpson, R. E.; Fons, P.; Kolobov, A. V.; Fukaya, T.; Krbal, M.; Yagi, T.; Tominaga, J. Interfacial Phase-Change Memory. *Nat. Nanotechnol.* **2011**, *6*, 501−505.

(10) Lee, T. H.; Loke, D.; Huang, K.-J. J.; Wang, W.-J. J.; Elliott, S. R. Tailoring Transient-Amorphous States: Towards Fast and Power-Efficient Phase-Change Memory and Neuromorphic Computing. *Adv. Mater.* **2014**, *26*, 7493−7498.

(11) Skelton, J. M.; Loke, D.; Lee, T.; Elliott, S. R. Ab Initio Molecular-Dynamics Simulation of Neuromorphic Computing in Phase-Change Memory Materials. *ACS Appl. Mater. Interfaces* **2015**, *7*, 14223−14230.

(12) Boybat, I.; Le Gallo, M.; Nandakumar, S. R.; Moraitis, T.; Parnell, T.; Tuma, T.; Rajendran, B.; Leblebici, Y.; Sebastian, A.; Eleftheriou, E. Neuromorphic Computing with Multi-Memristive Synapses. *Nat. Commun.* **2018**, *9*, 1−12.

(13) Shportko, K.; Kremers, S.; Woda, M.; Lencer, D.; Robertson, J.; Wuttig, M. Resonant Bonding in Crystalline Phase-Change Materials. *Nat. Mater.* **2008**, *7*, 653−658.

(14) Raoux, S.; Welnic, W.; Ielmini, D. Phase Change Materials and Their Application to Nonvolatile Memories. *Chem. Rev.* **2010**, *110*, 240−267.

(15) Peng, C.; Wu, L.; Song, Z.; Rao, F.; Zhu, M.; Li, X.; Liu, B.; Cheng, L.; Feng, S.; Yang, P.; et al. Performance Improvement of Sb_2Te_3 Phase Change Material by Al Doping. *Appl. Surf. Sci.* **2011**, *257*, 10667−10670.

(16) Liu, B.; Song, Z.; Feng, S.; Chen, B. Characteristics of Chalcogenide Nonvolatile Memory Nano-Cell-Element Based on Sb2Te3Material. *Microelectron. Eng.* **2005**, *82*, 168−174.

(17) Loke, D. K.; Skelton, J. M.; Lee, T. H.; Zhao, R.; Chong, T.-C. C.; Elliott, S. R. Ultrafast Nanoscale Phase-Change Memory Enabled By Single-Pulse Conditioning. *ACS Appl. Mater. Interfaces* **2018**, *10*, 41855−41860.

(18) Zhang, W.; Mazzarello, R.; Wuttig, M.; Ma, E. Designing Crystallization in Phase-Change Materials for Universal Memory and Neuro-Inspired Computing. *Nat. Rev. Mater.* **2019**, *4*, 150−168.

(19) Liu, B.; Liu, W.; Li, Z.; Li, K.; Wu, L.; Zhou, J.; Song, Z.; Sun, Z. Y-Doped Sb 2 Te 3 Phase-Change Materials: Toward a Universal Memory. *ACS Appl. Mater. Interfaces* **2020**, *12*, 20672−20679.

(20) Pries, J.; Wei, S.; Wuttig, M.; Lucas, P. Switching between Crystallization from the Glassy and the Undercooled Liquid Phase in Phase Change Material Ge2Sb2Te5. *Adv. Mater.* **2019**, *31*, 1900784.

(21) Zier, T.; Zijlstra, E. S.; Kalitsov, A.; Theodonis, I.; Garcia, M. E. Signatures of Nonthermal Melting. *Struct. Dyn.* **2015**, *2*, No. 054101.

(22) Bothschafter, E. M.; Paarmann, A.; Zijlstra, E. S.; Karpowicz, N.; Garcia, M. E.; Kienberger, R.; Ernstorfer, R. Ultrafast Evolution of the Excited-State Potential Energy Surface of TiO2 Single Crystals Induced by Carrier Cooling. *Phys. Rev. Lett.* **2013**, *110*, 1−5.

(23) Zijlstra, E. S.; Kalitsov, A.; Zier, T.; Garcia, M. E. Fractional Diffusion in Silicon. *Adv. Mater.* **2013**, *25*, 5605−5608.

(24) Rousse, A.; Rischel, C.; Fourmaux, S.; Uschmann, I.; Sebban, S.; Grillon, G.; Balcou, P.; Förster, E.; Geindre, J. P.; Audebert, P.; et al. Non-Thermal Melting in Semiconductors Measured at Femtosecond Resolution. *Nature* **2001**, *410*, 65−68.

(25) Kolobov, A. V.; Krbal, M.; Fons, P.; Tominaga, J.; Uruga, T. Distortion-Triggered Loss of Long-Range Order in Solids with Bonding Energy Hierarchy. *Nat. Chem.* **2011**, *3*, 311−316.

(26) Saeta, P.; Wang, J.-K.; Siegal, Y.; Bloembergen, N.; Mazur, E. Ultrafast Electronic Disordering during Femtosecond Laser Melting of GaAs. *Phys. Rev. Lett.* **1991**, *67*, 1023−1026.

(27) Shank, C. V.; Yen, R.; Hirlimann, C. Time-Resolved Reflectivity Measurements of Femtosecond-Optical-Pulse-Induced Phase Transitions in Silicon. *Phys. Rev. Lett.* **1983**, *50*, 454−457.

(28) Hada, M.; Oba, W.; Kuwahara, M.; Katayama, I.; Saiki, T.; Takeda, J.; Nakamura, K. G. Ultrafast Time-Resolved Electron Diffraction Revealing the Nonthermal Dynamics of near-UV Photo-excitation-Induced Amorphization in Ge2Sb2Te5. *Sci. Rep.* **2015**, *5*, 13530.

(29) Wang, Q. F.; Shi, L. P.; Huang, S. M.; Miao, X. S.; Wong, K. P.; Chong, T. C. Dynamics of Ultrafast Crystallization in As-Deposited Ge 2Sb 2Te 5 Films. *Japanese J. Appl. Physics, Part 1 Regul. Pap. Short Notes Rev. Pap.* **2004**, *43*, 5006−5008.

(30) Stampfli, P.; Bennemann, K. H. Dynamical Theory of the Laser-Induced Lattice Instability of Silicon. *Phys. Rev. B: Condens. Matter Mater. Phys.* **1992**, *46*, 10686−10692.

(31) Kolobov, A. V.; Krbal, M.; Fons, P.; Tominaga, J.; Uruga, T. Distortion-Triggered Loss of Long-Range Order in Solids with Bonding Energy Hierarchy. *Nat. Chem.* **2011**, *3*, 311−316.

(32) *CRC Handbook of Chemistry and Physics*, 95th ed.; Haynes, W. M., Ed.; CRC Press: Boca Raton, 2014.

(33) Dronskowski, R.; Bloechl, P. E. Crystal Orbital Hamilton Populations (COHP). Energy-Resolved Visualization of Chemical Bonding in Solids Based on Density-Functional Calculations. *J. Phys. Chem.* **1993**, *97*, 8617−8624.

(34) De Proft, F.; Van Alsenoy, C.; Peeters, A.; Langenaeker, W.; Geerlings, P. Atomic Charges, Dipole Moments, and Fukui Functions Using the Hirshfeld Partitioning of the Electron Density. *J. Comput. Chem.* **2002**, *23*, 1198−1209.

(35) Sosso, G. C.; Caravati, S.; Bernasconi, M. Vibrational Properties of Crystalline Sb2Te3 from First Principles. *J. Phys.: Condens. Matter* **2009**, *21*, 095410.

(36) Shakhvorostov, D.; Nistor, R. A.; Krusin-Elbaum, L.; Martyna, G. J.; Newns, D. M.; Elmegreen, B. G.; Liu, X. H.; Hughes, Z. E.; Paul,

S.; Cabral, C.; et al. Evidence for Electronic Gap-Driven Metal-Semiconductor Transition in Phase-Change Materials. *Proc. Natl. Acad. Sci. U. S. A.* **2009**, *106*, 10907−10911.
(37) Braun, L. Z. Electron and Phonon Dynamics in Topological Insulators at THz Frequencies. Free University Berlin, 2016.
(38) Kolobov, A. V.; Fons, P.; Tominaga, J.; Hase, M. Excitation-Assisted Disordering of GeTe and Related Solids with Resonant Bonding. *J. Phys. Chem. C* **2014**, *118*, 10248−10253.
(39) Lian, C.; Zhang, S. J.; Hu, S. Q.; Guan, M. X.; Meng, S. Ultrafast Charge Ordering by Self-Amplified Exciton−Phonon Dynamics in TiSe2. *Nat. Commun.* **2020**, *11*. DOI: 10.1038/s41467-019-13672-7
(40) Harb, M.; Ernstorfer, R.; Hebeisen, C. T.; Sciaini, G.; Peng, W.; Dartigalongue, T.; Eriksson, M. A.; Lagally, M. G.; Kruglik, S. G.; Miller, R. J. D. Electronically Driven Structure Changes of Si Captured by Femtosecond Electron Diffraction. *Phys. Rev. Lett.* **2008**, *100*, 1−4.
(41) Siders, C. W.; Cavalleri, A.; Sokolowski-Tinten, K.; Tóth, C.; Guo, T.; Kammler, M.; Horn Von Hoegen, M.; Wilson, K. R.; Von Der Linde, D.; Barty, C. P. J. Detection of Nonthermal Melting by Ultrafast X-Ray Diffraction. *Science (Washington, DC, U. S.)* **1999**, *286*, 1340−1342.
(42) Rao, F.; Ding, K.; Zhou, Y.; Zheng, Y.; Xia, M.; Lv, S.; Song, Z.; Feng, S.; Ronneberger, I.; Mazzarello, R.; et al. Reducing the Stochasticity of Crystal Nucleation to Enable Subnanosecond Memory Writing. *Science (Washington, DC, U. S.)* **2017**, *358*, 1423−1427.
(43) Loke, D.; Lee, T. H.; Wang, W. J.; Shi, L. P.; Zhao, R.; Yeo, Y. C.; Chong, T. C.; Elliott, S. R. Breaking the Speed Limits of Phase-Change Memory. *Science (Washington, DC, U. S.)* **2012**, *336*, 1566−1569.
(44) Cheng, Y.; Teitelbaum, S. W.; Gao, F. Y.; Nelson, K. A. Femtosecond Laser Amorphization of Tellurium. *Phys. Rev. B: Condens. Matter Mater. Phys.* **2018**, *134112*, 1−5.
(45) Waldecker, L.; Miller, T. A.; Rudé, M.; Bertoni, R.; Osmond, J.; Pruneri, V.; Simpson, R. E.; Ernstorfer, R.; Wall, S. Time-Domain Separation of Optical Properties from Structural Transitions in Resonantly Bonded Materials. *Nat. Mater.* **2015**, *14*, 991−995.
(46) Zhu, M.; Cojocaru-Mirédin, O.; Mio, A. M.; Keutgen, J.; KüPers, M.; Yu, Y.; Cho, J. Y.; Dronskowski, R.; Wuttig, M. Unique Bond Breaking in Crystalline Phase Change Materials and the Quest for Metavalent Bonding. *Adv. Mater.* **2018**, *30*, 1706735.
(47) Raty, J. Y.; Schumacher, M.; Golub, P.; Deringer, V. L.; Gatti, C.; Wuttig, M. A Quantum-Mechanical Map for Bonding and Properties in Solids. *Adv. Mater.* **2019**, *31*, 1−6.
(48) Papoian, G. A.; Hoffmann, R. Hypervalent Bonding in One, Two, and Three Dimensions: Extending the Zintl-Klemm Concept to Nonclassical Electron-Rich Networks. *Angew. Chem., Int. Ed.* **2000**, *39*, 2408−2448.
(49) Klemenz, S.; Hay, A. K.; Teicher, S. M. L.; Topp, A.; Cano, J.; Schoop, L. M. The Role of Delocalized Chemical Bonding in Square-Net-Based Topological Semimetals. *J. Am. Chem. Soc.* **2020**, *142*, 6350−6359.
(50) Shimojo, F.; Fukushima, S.; Kumazoe, H.; Misawa, M.; Ohmura, S.; Rajak, P.; Shimamura, K.; Bassman, L.; Tiwari, S.; Kalia, R. K.; et al. QXMD: An Open-Source Program for Nonadiabatic Quantum Molecular Dynamics. *SoftwareX* **2019**, *10*, 100307.
(51) Hohenberg, P.; Kohn, W. Inhomogeneous Electron Gas. *Phys. Rev.* **1964**, *136*, B864−B871.
(52) Car, R.; Parrinello, M. Unified Approach for Molecular Dynamics and Density-Functional Theory. *Phys. Rev. Lett.* **1985**, *55*, 2471−2474.
(53) Kohn, W.; Sham, L. J. Self-Consistent Equations Including Exchange and Correlation Effects. *Phys. Rev.* **1965**, *140*, A1133−A1138.
(54) Kohn, W.; Vashishta, P. General Density Functional Theory. *Theory Inhomogeneous Electron Gas* **1983**, 79−147.
(55) Shimojo, F.; Ohmura, S.; Mou, W.; Kalia, R. K.; Nakano, A.; Vashishta, P. Large Nonadiabatic Quantum Molecular Dynamics Simulations on Parallel Computers. *Comput. Phys. Commun.* **2013**, *184*, 1−8.
(56) Perdew, J. P.; Burke, K.; Ernzerhof, M. Generalized Gradient Approximation Made Simple. *Phys. Rev. Lett.* **1996**, *77*, 3865−3868.
(57) Grimme, S. Semiempirical GGA-Type Density Functional Constructed with a Long-Range Dispersion Correction. *J. Comput. Chem.* **2006**, *27*, 1787−1799.
(58) Blöchl, P. E. Projector Augmented-Wave Method. *Phys. Rev. B: Condens. Matter Mater. Phys.* **1994**, *50*, 17953−17979.
(59) Tully, J. C. Molecular Dynamics with Electronic Transitions. *J. Chem. Phys.* **1990**, *93*, 1061−1071.
(60) Casida, M. E. *Recent Advances in Density Functional Methods*; Chong, D. P., Ed.; Recent Advances in Computational Chemistry; World Scientific Publishing Co. Pte. Ltd., 1995.
(61) Shimojo, F.; Ohmura, S.; Mou, W.; Kalia, R. K.; Nakano, A.; Vashishta, P. Large Nonadiabatic Quantum Molecular Dynamics Simulations on Parallel Computers. *Comput. Phys. Commun.* **2013**, *184*, 1−8.

https://dx.doi.org/10.1021/acs.jpclett.0c02521
J. Phys. Chem. Lett. 2020, 11, 10242−10249